Patterns and Intensities of Near-Infrared and Short-Wavelength Fundus Autofluorescence in Choroideremia Probands and Carriers

Maarjaliis Paavo,[1,2] Jose R. L. Carvalho Jr,[1,3,4] Winston Lee,[1] Jesse D. Sengillo,[1,5] Stephen H. Tsang,[1,6] and Janet R. Sparrow[1,6]

[1]Department of Ophthalmology Columbia University Medical Center, New York, New York, United States
[2]Department of Ophthalmology, Helsinki University Hospital, Helsinki, Finland
[3]Department of Ophthalmology, Empresa Brasileira de Servicos Hospitalares, Hospital das Clinicas de Pernambuco, Federal University of Pernambuco, Recife, Brazil
[4]Department of Ophthalmology, Federal University of São Paulo, São Paulo, Brazil
[5]Department of Internal Medicine, Reading Hospital of Tower Health, West Reading, Pennsylvania, United States
[6]Department of Pathology and Cell Biology, Columbia University Medical Center, New York, New York, United States

Correspondence: Janet R. Sparrow, Department of Ophthalmology, Columbia University Medical Center, 635 W. 165th Street, New York, NY 10032, USA; jrs88@cumc.columbia.edu.

Submitted: April 19, 2019
Accepted: August 3, 2019

Citation: Paavo M, Carvalho JRL Jr, Lee W, Sengillo JD, Tsang SH, Sparrow JR. Patterns and intensities of near-infrared and short-wavelength fundus autofluorescence in choroideremia probands and carriers. *Invest Ophthalmol Vis Sci*. 2019;60:3752–3761. https://doi.org/10.1167/iovs.19-27366

Purpose. To ascertain cellular constituents within islands of preserved retina in choroideremia (CHM) by multimodal imaging.

Methods. CHM probands (16) and female carriers (9) of CHM were studied. Near-infrared autofluorescence (NIR-AF; 787-nm excitation; emission, >830 nm), short-wavelength autofluorescence (SW-AF; 488-nm excitation, 500- to 680-nm emission), and spectral-domain optical coherence tomography (SD-OCT) images were acquired with a confocal scanning laser ophthalmoscope. SW-AF intensities were measured by quantitative fundus autofluorescence (qAF), and NIR-AF intensity profiles were analyzed. Retinal thicknesses and visual acuity were measured.

Results. In 19 of 31 eyes of affected males, islands of preserved NIR-AF signal were also visible as fluorescence signal in SW-AF images. Notable in 12 eyes were areas of speckled SW-AF that was hypoautofluorescent in the NIR-AF image. Islands of preserved NIR-AF and SW-AF signal were often associated with the presence of visible but thinned outer nuclear layer and discontinuous interdigitation zone, ellipsoid zone, and external limiting membrane. NIR-AF profiles revealed that even in areas of preserved retina, the NIR-AF signal from retinal pigment epithelium (RPE) melanin is greatly reduced. qAF was reduced overall. The fundus of carriers was characterized by a mosaicism in which patches of reduced NIR-AF colocalized with reduced SW-AF.

Conclusions. In CHM-affected males, the presence of RPE was indicated by an NIR-AF signal and the absence of hypertransmission of OCT signal into the choroid. RPE preservation was associated with better visual acuity. In carriers, patches of reduced SW-AF colocalized with decreased NIR-AF and qAF was severely reduced.

Keywords: X-linked choroideremia, quantitative fundus autofluorescence, near-infrared autofluorescence

Choroideremia (CHM) is an X-linked recessive disorder that affects ~1 in 50,000 individuals[1] and is characterized by the progressive degeneration of photoreceptor cells, retinal pigment epithelium (RPE), and the underlying choroid in affected males. CHM typically has onset in juveniles and is attributable to pathogenic variants in the *CHM* gene (OMIM 300390)[2,3] that encodes the ubiquitously expressed Rab escort protein 1 (REP-1)[4] expressed by rods and RPE.[5] REP1 participates in the lipid modification (prenylation) of Rab GTPases. The latter are vital regulators of intracellular vesicular transport and organelle movement. The deficiency in REP1 can be compensated for by REP2 in most cell types but, as evidenced by CHM, adequate compensation does not occur in retina[6,7]; the result is widespread chorioretinal atrophy.[8,9] One of the Rabs affected in CHM is Rab27a, which is required for melanosome movement into the apical processes of RPE cells.[10]

Disease-associated variants in *CHM* consist predominantly of null or loss-of-function alleles[2]; however, phenotypes can vary across individuals. Disease onset in affected males is generally marked by slowed dark adaptation, followed by progressive constriction of the visual field and degeneration of RPE, choroid, and photoreceptor cells. Spectral-domain optical coherence tomography (SD-OCT) imaging of affected males has revealed zones of macular sparing bordered by the loss of interdigitation zone (IZ) and ellipsoid zone (EZ), with outer nuclear layer (ONL) thinning, and increased signal transmission posterior to RPE/Bruch's membrane.[11–13] Foveal structure and function can be retained for several decades.[12–15]

Investigative Ophthalmology & Visual Science

Heterozygous female carriers of CHM mutations are typically asymptomatic. However, some carriers report nyctalopia in middle and late life, and full-field electroretinography (ERG) recordings can be abnormal.[16–18] In short-wavelength autofluorescence (SW-AF) images, patches of hyperautofluorescence alternate with hypoautofluorescence,[17–19] a mosaicism that is considered to reflect random X-inactivation. By multifocal ERG, abnormal responses corresponding to the mosaic pattern can be recorded.[19,20] In SD-OCT scans, female carriers occasionally present with hyperreflective foci that interrupt photoreceptor-attributable bands and correspond to hyperautofluorescent foci in the macula.[11,17]

Despite histopathologic studies,[21] in vivo imaging, and the availability of mouse models,[22,23] it remains uncertain as to whether degeneration is initiated in photoreceptor cells[5,13,24] or RPE[25–29] or whether it is a simultaneous process in both cell types.[30] A more consistent observation is that the loss of choroidal tissue occurs secondary to the degeneration of RPE and photoreceptors rather than being the site of the primary changes.[5]

Gene replacement therapy for the treatment of CHM is currently being explored[31–33] (ClinicalTrials.gov numbers, NCT02553135, NCT02407678, and NCT02341807), and recent results from a phase 1/2 clinical trial indicate that persistent, clinically significant visual acuity gains can be achieved in eyes in which rapid visual acuity loss would otherwise be expected.[34] The aim of this study was to correlate SW-AF and near-infrared fundus autofluorescence (NIR-AF) signal with SD-OCT images in affected males and female carriers of CHM to better identify the cellular constituents in preserved central islands of the retina. In the healthy eye, SW-AF and NIR-AF are primarily generated in RPE cells, with SW-AF emission originating from retinal bisretinoid lipofuscin and NIR-AF from RPE melanin.[35,36] We have also implemented quantitative approaches to analyze SW-AF by quantitative fundus autofluorescence (qAF) and to measure NIR-AF intensities.

Methods

Patients, Clinical Evaluation, and Genetic Testing

A retrospective observational study of images acquired from patients presenting to the Department of Ophthalmology Columbia University was performed. Institutional review board/ethics committee approval was obtained under protocol AAAR8743. All study-related procedures adhered to the tenants established in the Declaration of Helsinki.

All patients underwent a comprehensive ophthalmic examination by a retina specialist (SHT). The fundus was examined under pupillary dilatation and best corrected visual acuity (BCVA) was determined. The diagnosis of CHM in probands was based on clinical findings and confirmed by direct sequencing of the CHM gene. Heterozygous female carriers were identified through affected probands (relatives) and subsequently screened for the causative heterozygous mutation.

Image Acquisition and Analysis

NIR-AF images (30° and 50° field, 787-nm excitation, >830-nm emission without injection of dye) were captured with Heidelberg retinal tomography 2-scanning laser ophthalmoscope (Heidelberg Engineering, Heidelberg, Germany). For NIR-AF quantification, nonnormalized 30° × 30° images acquired at a fixed sensitivity of 96 (available for 9 probands and 3 CHM carriers) were analyzed using open source software (Fiji; National Institutes of Health, Bethesda, MD, USA). Pixel gray levels were determined at 0.25-mm intervals along a horizontal line through the fovea, and profiles were aligned. The gray level values were then adjusted by subtracting the NIR-AF image gray level offset value provided by the Heidelberg software. The mean and 95% confidence intervals (CIs) were plotted as a distance along the x axis in the temporal (0 to −4 mm) and nasal (0 to +4 mm) direction relative to the fovea, and a comparison was made to 19 healthy subjects as previously described.[37] The healthy cohort consisted of subjects without eye disease, the mean age was 35.3 ± 9.4 SD years (range, 12.7–52.7 years), and 10 subjects identified themselves as Caucasian, with 3 as Hispanic, 4 Asian, and 2 African American. SW-AF (blue autofluorescence; 488-nm excitation, 500- to 680-nm emission) images (30° × 30° fields) were acquired with a modified confocal scanning laser ophthalmoscope (Spectralis HRA+OCT; Heidelberg Engineering) in automatic real-time tracking capture mode. qAF was measured at an eccentricity of 7° to 9° with normalization as previously described.[38] An analysis of a fixed foveal segment (1°) in both patients and controls was also performed. A comparison was made to a normative database of healthy eyes (374 eyes; age range, 5–65 years).[38]

SD-OCT line and volume scans in high-resolution mode and a corresponding infrared reflectance fundus image were acquired with a confocal scanning laser ophthalmoscope (Spectralis HRA+OCT; Heidelberg Engineering). Foveal thickness (FT) and subfoveal choroidal thickness (SFT) were manually measured using the caliper tool in the Heidelberg Explorer (HEYEX) software. FT was defined as the distance from the internal limiting membrane to the outer border of RPE-Bruch's membrane and SFT as the distance between the outer border of the RPE-Bruch's membrane complex and the choriosclera border under the fovea.

Color fundus photographs were obtained with a FF 450plus Fundus Camera (Carl Zeiss Meditec, Jena, Germany). Ultra-widefield (200°) high-resolution Optomap images were captured with Optos (Optos Daytona; Optos, Inc., Marlborough, MA, USA) in the composite pseudocolor and green autofluorescence (excitation 532 nm) mode.

Statistical Analysis

Statistical analyses were performed using the Prism 5 software (GraphPad Software, La Jolla, CA, USA) and the statistical tests as indicated. Statistical significance was evaluated by comparing CIs and by Wilcoxon-Mann-Whitney Test as appropriate. The Bland-Altman analysis was used to assess interobserver agreement.

Results

Fundus Imaging in Affected Patients

The study cohort consisted of 16 affected patients (31 eyes); one eye of one patient was excluded because the advanced stage of CHM precluded the acquisition of NIR-AF and qAF images. All affected patients were male with a mean age of 44.9 years (range, 10.2–77.2) at the time of examination. BCVA ranged from 20/20 to 20/150 (Table). Demographic, clinical, and genetic data along with familial relationships are summarized in the Table. All images were evaluated independently by two investigators (MP, JRS). Disease-causing mutations in the CHM gene were detected in all affected patients and carriers who underwent genetic screening. P9 and C4 were not screened but were clinically diagnosed and reported a positive family history of CHM, respectively. In total, 19 unique variants

Table. Demographic, Clinical, and Genetic Characteristics of Affected Patients and Heterozygous Carriers of the Choroideremia Study Cohort

Patient Number	Age (y)	Sex	Race/Ethnicity	LogMAR BCVA OD	LogMAR BCVA OS	Study Eye	*CHM* Variant* cDNA (Protein)	Zygosity	Relationship
P1	43	M	Caucasian	0.00	0.79	OU	c.877C>T (p.Arg293†)	Hemizygous	Proband
P2	52	M	African-American	0.30	0.30	OU	c.49+1G>A (p.?)	Hemizygous	Proband
P3	46	M	Caucasian	0.87	0.79	OU	c.1349G>T (p.Arg450Met)	Hemizygous	Proband
P4	36	M	Caucasian	0.30	0.00	OU	c.315-2A>G (p.?)	Hemizygous	Proband
P5	68	M	Caucasian	0.39	0.30	OU	c.1771-1G>A (p.?)	Hemizygous	Proband
P6	28	M	African-American	0.30	0.17	OU	Deletion of Exon 12‡	Hemizygous	Proband
P7	57	M	Caucasian	0.00	0.20	OU	c.82del (Ser28Glnfs†32)	Hemizygous	Proband
P8	58	M	Caucasian	0.47	0.40	OU	c.1520A>G (p.His507Arg)	Hemizygous	Proband
P9	60	M	African-American	0.10	0.10	OU	Not screened	Hemizygous	Proband
P10	31	M	Iranian	0.80	0.00	OU	c.1237_1328del (p.Ser413Valfs†18)	Hemizygous	Proband
P11	77	M	Caucasian	0.40	0.60	OU	Deletion of Exons 6 and 7‡	Hemizygous	Proband
P12	51	M	Caucasian	0.40	0.40	OU	c.1580_1584del (p.Leu527Cysfs†5)	Hemizygous	Proband
P13	52	M	Caucasian	0.10	0.10	OS	Deletion of Exons 9 and 10‡	Hemizygous	Proband
P14	21	M	Caucasian	0.00	0.10	OU	c.1584_1587del (p.Val529Hisfs†7)	Hemizygous	Proband
P15	31	M	Caucasian/North-African	0/0	0.00	OU	c.819+1G>A (p.?)	Hemizygous	Proband
P16	10	M	Indian	0.10	0.10	OU	Deletion of entire *CHM* locus‡	Hemizygous	Proband
Carrier									
C1	53	F	Caucasian	0.30	0.30	OU	c.1584_1587del (p.Val529Hisfs†7)	Heterozygous	Sister (P14)
C2	51	F	African-American	0.10	1.00	OU	c.1349G>T (Arg450Met)	Heterozygous	Sister (P3)
C3	76	F	Caucasian	0.10	0.10	OU	c.49+1G>A (p.?)	Heterozygous	Mother (P2)
C4	49	F	African-American	0.00	0.00	OU	Not screened	Heterozygous	
C5	49	F	African-American	0.00	0.00	OU	Deletion of Exon 12‡	Heterozygous	Mother (P6)
C6	61	F	Caucasian	0.50	0.47	OU	c.757C>T (p.Arg253†)	Heterozygous	
C7	65	F	Caucasian	0.10	0.30	OU	c.1584_1587del (p.Val529Hisfs†7)	Heterozygous	
C8	54	F	Caucasian	0.00	0.17	OU	c.189G>C (p.Gln63His)	Heterozygous	
C9	29	F	Hispanic	0.00	0.00	OU	c.940G>A (p.Gly314Arg)	Heterozygous	

P, patients; C, carrier; M, male; F, female; OD, right eye; OS, left eye; OU, both eyes.
* GRCh38 assembly/NM_000390.3.
† Nonsense mutation.
‡ Failure of amplification by polymerase chain reaction.

were detected in the cohort (Supplementary Table S1), the majority of which were frameshifts (26.3%), large deletions (21.1%), and non-coding or intronic (26.3%). All intronic mutations occurred within canonical splice sites (±1 and ±2) and are strongly predicted to result in skipping of the subsequent or adjacent exon. All missense variants are predicted to be pathogenic or previously associated with CHM (single nucleotide polymorphism).

Patients exhibited varying degrees of chorioretinal atrophy. In color fundus photographs, regions of advanced degeneration and widespread depigmentation were pale due to the reflection of light from bare sclera (Fig. 1A: proband/patient 7 [P7], white asterisk). In areas of exposed choroid, pigment and choroidal vessels were visible (Fig. 1 A: P7, P5). The choroidal vessel patterns visible in the color fundus photographs typically matched similar patterns in NIR-AF images (Figs. 1A and B: P7, P5). In areas of outer retinal atrophy, choroidal vessels were outlined by the diffuse NIR-AF emanating from residual choroidal pigment (Fig. 1B: P7, P5, P15, P6).

In 8 patients (13 eyes), distinct islands of preserved RPE in NIR-AF images presented as NIR-AF situated anterior to choroidal vessels (Fig. 1B: P7, P5, and P15 as green, yellow, and red asterisks, respectively). In another 3 patients (6 eyes), NIR-AF presented as foci of a more limited size. In 23 eyes for which color fundus photographs were available, 9 eyes served as examples in which islands of NIR-AF colocalized with pigmented zones in color fundus photographs. These islands were either dense (Fig. 1B: P5, green asterisk) or less compacted (Fig. 1B: P7, green asterisk). In 19 of 31 eyes, preserved NIR-AF signal was also visible as fluorescence signal in SW-AF images (Figs. 1B and 1C: P7, P5, and P15; green and yellow asterisks in figure panels). However, in the remaining 12 eyes (6 patients), nummular pigment visible in color fundus photographs and NIR-AF images was remarkably dark in SW-AF images (Fig. 1B, 1C: P7, P6, red asterisks) and, as discussed below, was typically associated with thinning of outer retina.

Also notable in 12 eyes and illustrated for P6 was a large area of speckled SW-AF that was hypoautofluorescent in the NIR-AF image (Figs. 1B, 1C: P6, blue asterisk). Similarly, in P5, the central island of residual AF included finger-like extensions that exhibited signal in the SW-AF image but not in the NIR-AF image (Fig. 1C: P5, blue arrowhead). The presence of pigment in color photographs that corresponds to a weak signal in NIR-AF images (Fig. 1A–C: P5, white arrow) may be indicative of choroidal melanin.

In SD-OCT scans, areas of severe chorioretinal atrophy were defined by an absence of photoreceptor-attributable reflectivity bands (Fig. 1D: P7, white asterisk and bracket). Areas of RPE loss and absent outer retinal bands were also associated with hyporeflectance and could be identified by increased signal transmission into the choroid; the latter was visible as vertical streaks extending posterior to RPE/Bruch's membrane (Fig. 1D: P7, purple arrowheads). In some of these areas, the choroid had also atrophied. With severe outer retinal degeneration, the reflectivity layer attributable to inner nuclear layer descended into the gap (Fig. 1D: P6, red arrow).

On the other hand, islands presenting with preserved NIR-AF and SW-AF signals were often associated with the presence of a visible but thinned ONL, nondetectable IZ and EZ, and external limiting membrane (ELM) that were discernible to

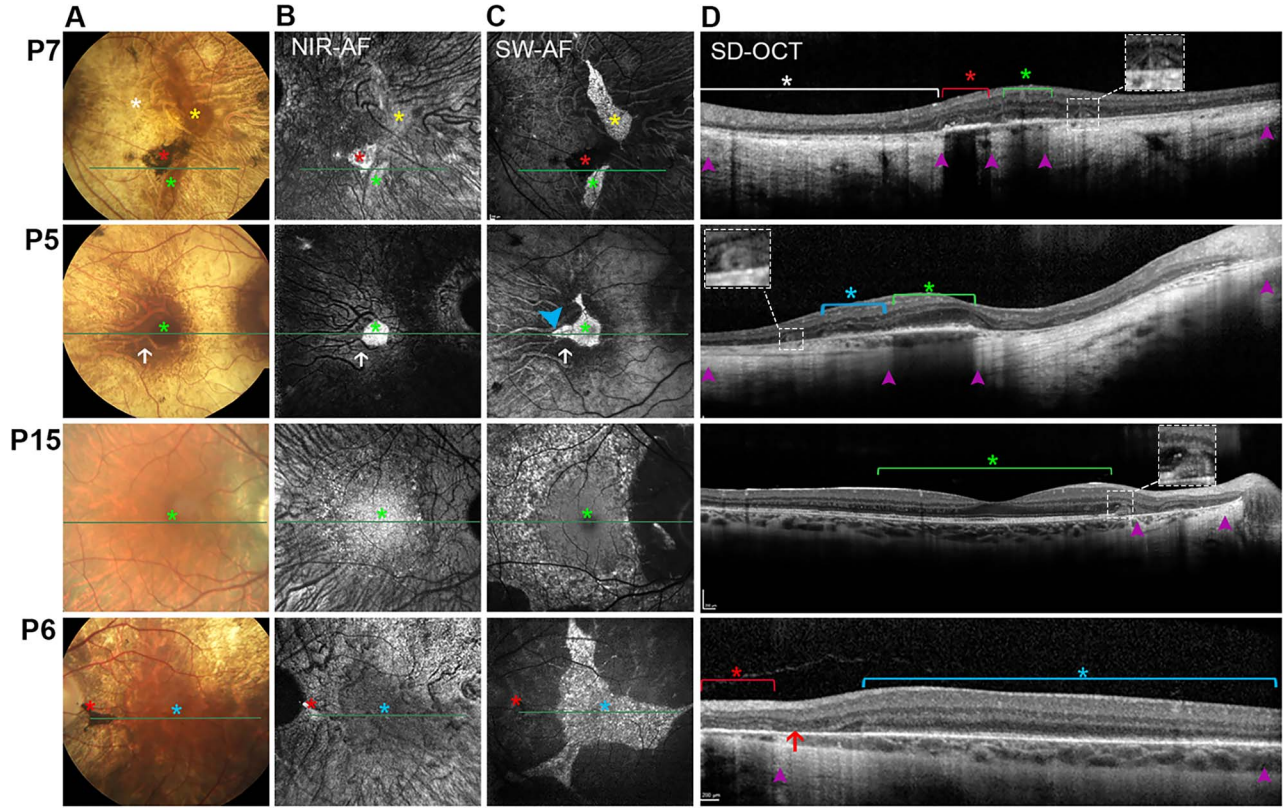

Figure 1. Multimodal fundus imaging of CHM probands (patients P7, P5, P15, and P6). Color fundus photographs (**A**) NIR-AF (**B**), SW-AF (**C**), and SD-OCT (**D**) reveal islands exhibiting NIR-AF and SW-AF signals (*green* and *yellow asterisk*); residual pigment and NIR-AF signal devoid of SW-AF (*red asterisk*); bare sclera (*white asterisks*); SW-AF signal in the absence of NIR-AF (*blue asterisk*, *blue arrow*); and hypertransmission of OCT signal (*pink arrowhead*). In P5, retained pigment in **A** exhibits weak NIR-AF but no SW-AF (*white arrow*). In P6, severe outer retinal degeneration exists with inner nuclear layer descent (*red arrow*). In SD-OCT scans (**D**) brackets indicate the corresponding area in the NIR-AF and SW-AF image. The horizontal axis and extent of the corresponding SD-OCT image are indicated by the *green lines* in **A**–**C**.

variable extents or absent (Fig. 1D: P7, P5, P15, green bracket). In the SD-OCT scan presented for P7, outer retinal tubulations (ORTs) were visible in an island that exhibited NIR-AF signal but was devoid of SW-AF (Fig. 1D: P7, red asterisk). Here, hyperreflectivity associated with the dense pigment reduced transmission of the OCT signal into the choroid (Fig. 1D: P7, red asterisk). Foci of the SW-AF signal in the absence of NIR-AF appeared to be associated with thinned ONL and discontinuous or loss of IZ, EZ, and ELM bands along, with hypertransmission into the choroid (Fig. 1C: P5, AF blue arrowhead; D: P5, blue asterisk).

Preservation of the fovea and parafovea as exhibited by P15 was identified by the increased central NIR-AF signal and decreased foveal SW-AF, both of which are characteristic of the macula in healthy eyes (Fig. 1B, 1C: P15). In addition, the SD-OCT image revealed a relatively intact outer retina (Fig. 1D: P15, green bracket). Of additional interest is the speckled autofluorescence that characterized the extrafoveal region in the SW-AF image. This brightly speckled macular area in the SW-AF image was hypoautofluorescent in the NIR-AF image (Figs. 1B, 1C: P15).

Fundus Imaging in CHM Carriers

Nine heterozygous carriers were also included in the study (18 eyes). The mean age in the carrier group was 54 (29.3–75.5) and visual acuity ranged from 20/20 to 20/200 (Table).

In SW-AF and NIR-AF images, 9 carriers (18 eyes) exhibited AF mottling with mosaic-like patterns of alternating hypo- and iso-AF extending throughout the posterior pole (18/18 eyes) (Figs. 2B, 2C). The areas of reduced NIR-AF in the mosaicism colocalized with foci of reduced SW-AF, although the contrast between hypo- and hyper-AF signal in the NIR-AF images was more pronounced than the contrast in corresponding areas in the SW-AF images (Figs. 2B1, 2C1).

Carrier 3 presented with more advanced peripapillary and macular atrophy in the color fundus image (Fig. 2D, carrier 3), with nummular areas of reduced NIR-AF and SW-AF signal (Fig. 2B, carrier 3). In SD-OCT scans acquired from carrier 3, thinning of the outer retina was readily observable as was an ORT and hypertransmission into the choroid (Fig. 2A, carrier 3). In all 9 carriers, hyperreflective disturbances of the EZ and IZ were observed in the SD-OCT scans, and hypertransmission into the choroid could be observed in association with these irregularities (Fig. 2A, carrier 1). These aberrations were also visible as bright hyperautofluorescent flecks in both SW-AF and NIR-AF images (Fig. 2B, carriers 1 and 2).

qAF in CHM-Affected Probands

To assess SW-AF intensities, qAF levels were measured in those patients for whom qAF imaging was available (6 affected patients, 7 eyes; P1, P5, P7, P9, P10, and P15; age, 31–67 years) and who exhibited foveal sparing. To better visualize the distribution of SW-AF intensities in relation to the central retinal islands, we constructed qAF maps (scaled from 0-1200 qAF units) and compared CHM patients to age-matched healthy eyes. The distribution of qAF signal in the CHM-affected patients (Fig. 3A: P15, P6, P10) was nonuniform and distinctly different than in the healthy age-similar eyes (Fig. 3C).

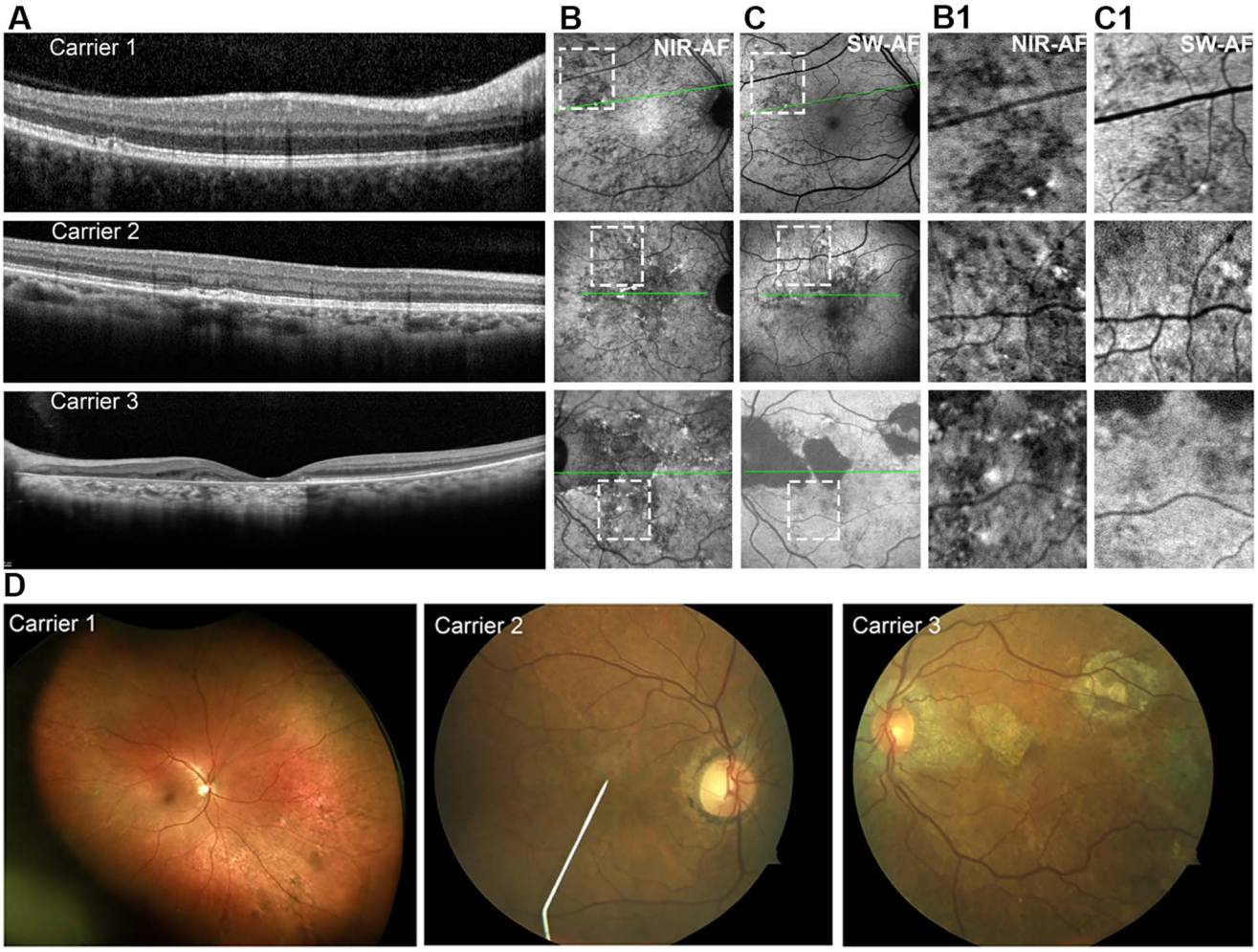

FIGURE 2. Multimodal imaging of choroideremia carriers (C1, C2, and C3). SD-OCT (**A**), NIR-AF (**B**), and SW-AF (**C**). Areas in the *rectangles* in **B** and **C** are expanded in **B1** and **C1**, respectively. The horizontal axis and extent of the corresponding SD-OCT image are indicated by the *green lines* in **B** and **C**. Fundus color photos are presented in the *lower panel* (**D**).

Specifically, throughout the macula, qAF was profoundly reduced in the probands not just in the areas of choreoretinal atrophy but also in the central areas of spared retina. Measurements were acquired within a foveal segment (1°). In both fundus zones, the qAF values of the probands were either within or below the range of the lower 95% CI in healthy eyes (Fig. 3D).

qAF in CHM Carriers

Short wavelength fundus autofluorescence was measured by qAF in 6 carriers (carriers 1, 4, 5, 7, 8, and 9; 12 eyes; age, 29–65 years) for whom qAF images were available. Color-coded qAF images revealed both an overall decrease in qAF and local increases and decreases associated with the mosaicism of the fundus (Figs. 4A, 4B: carriers 4, 1, and 5). SW-AF levels within the macula (qAF_8) in the eyes of heterozygous carriers fell below or within the lower limits (95% CI) of qAF levels in healthy eyes (Fig. 4D).

Quantitation of NIR-AF in Patients and Carriers

A semiquantitative analysis of NIR-AF intensities was performed using images acquired from 9 probands (P6, P7, P9, P10, P11, P12, P14, P15, and P16; 18 eyes; age, 10.2–77.2 years) and 3 carriers (C7, C8, and C9; 6 eyes; age range, 29.3–64.7 years). Intensities extracted from horizontal NIR-AF profiles through the fovea (Figs. 5A, 5B), revealed that for CHM probands, the mean NIR-AF intensity was below the 95% CI for healthy eyes (Fig. 5C, green trace versus red and yellow). Each NIR-AF profile spanned atrophic regions and islands of preserved tissue, thereby representing the signal from both exposed choroid and relatively preserved RPE. Notably, even in the central portions of the profiles corresponding to residual retina, the NIR-AF signal was below the normal range (Fig. 5C). Profiles of probands with central islands not visibly detectable in NIR-AF images (Figs. 5B, yellow trace; 5C, NIR-AF–) fell below the 95% CI of probands with a preserved island emitting detectable NIR-AF signal (Figs. 5A, red profile; 5C, NIR-AF+). Profiles of the carriers (Fig. 5C: blue trace) showed variability, with the central foveal values being below the healthy 95% CI (Fig. 5C, below, green trace).

Retinal Thickness and Visual Acuity in Relation to NIR-AF Signal

FT and SFT were measured in all 16 probands (31 eyes). In the group with detectable NIR-AF signal emitted from the retinal island, the average (±SD) FT and SFT were higher (FT, 191.6 μm ± 52.06; SFT, 148.42 ± 81.8) than in those with no NIR-AF signal originating from the central island (FT, 155.08 ± 102.5;

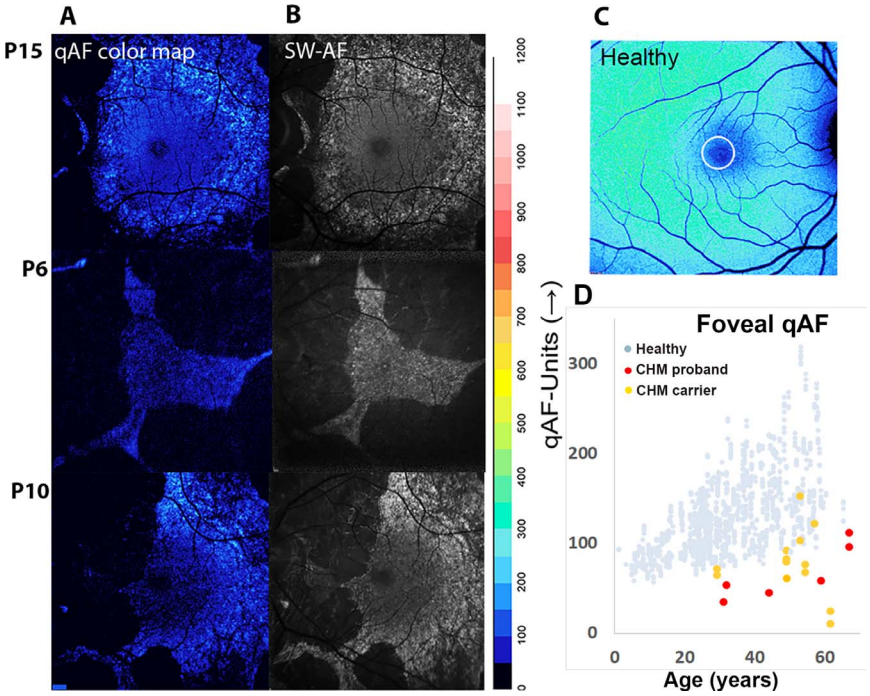

Figure 3. qAF color-coded images of P15, P6, and P10 (**A**). Corresponding SW-AF images (**B**). Healthy age-similar qAF color-coded image (**C**). qAF values acquired from foveal area (1° eccentricity; *circle* in **C**) and plotted as a function of age for healthy subjects (*blue circles*), CHM probands (P1, P5, P7, P9, P10, and P15; *red circles*), and CHM carriers (carriers 1, 3, 4, 7, 8, and 9; *yellow circles*) (**D**).

SFT, 124.6 ± 74.3); however, that difference was not statistically significant ($P = 0.21$ and $P = 0.58$, Wilcoxon-Mann-Whitney Test). The Bland-Altman analysis (Supplementary Fig. S1A) of the FT measurements obtained from the two observers revealed the mean of the differences to be 6.23 (±15.21, SD of the difference between the observers). The 95% limits of agreement between observers (estimated as $\pm 1.96 \times$ SD) were −23.6 to 36.0, indicating that measurements by observer 1 could be 23.6 units below or 36 units above observer 2. In the case of choroidal thickness (Supplementary

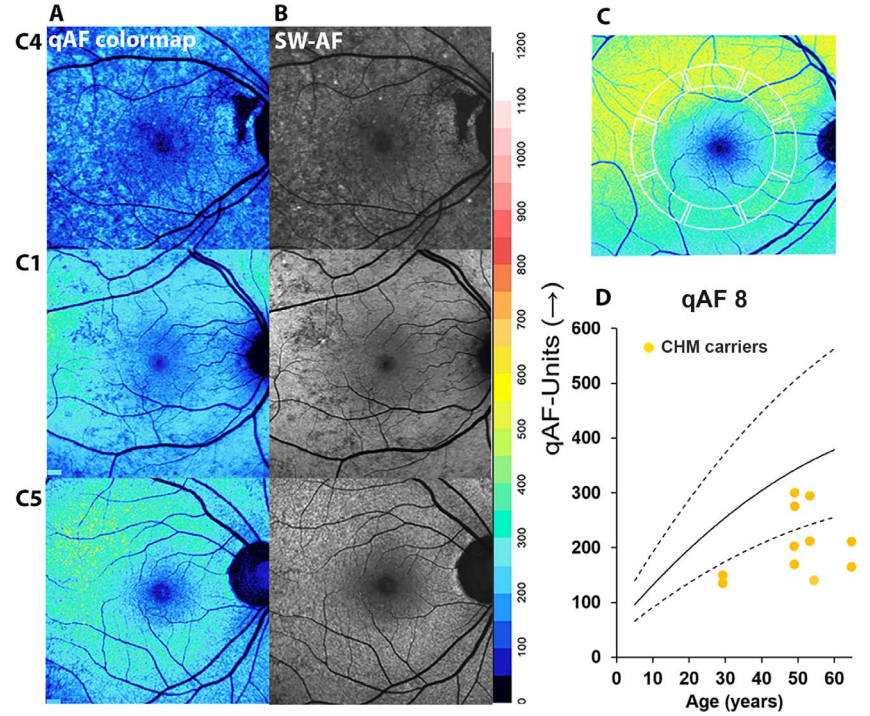

Figure 4. qAF in CHM carriers. qAF color-coded images of CHM carrier 4, carrier 1, and carrier 5 (**A**). Corresponding SW-AF images (**B**). Healthy (age 55 years) qAF color-coded image (**C**). qAF_8 values (*yellow circles*) acquired from 8 concentric segments (7°–9° eccentricity; outlined in **C**) and plotted as a function of age for carriers 1, 4, 5, 7, 8, and 9 (**D**). Mean (*solid black line*) ± 95% CIs (*dashed lines*).

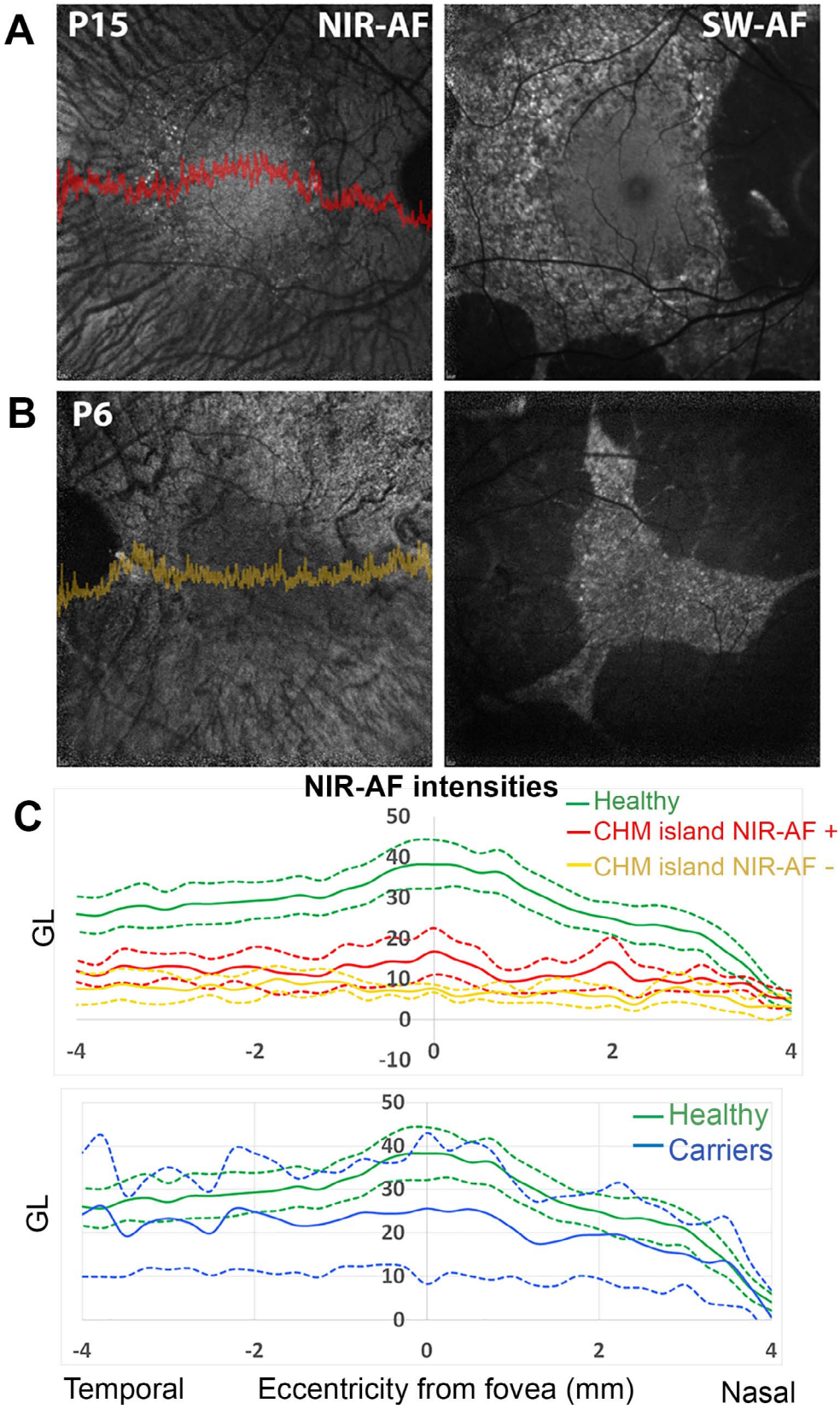

Figure 5. NIR-AF signal intensity profiles for CHM probands and carriers. NIR-AF images with profile overlay and SW-AF images for P15 (**A**) and P6 (**B**). Intensity profiles are presented as mean (*solid line*) and 95% CIs (*dashed line*). Horizontal intensity profiles through the fovea are shown for 6 patients exhibiting a central NIR-AF signal (NIR-AF+; *red profile*) and for 3 patients having reduced or absent central NIR-AF signal (NIR-AF–; *yellow profile*). Comparison is made to intensity profile constructed from 19 healthy eyes (*green profile*) (**C**, *above*). Horizontal profiles through the fovea are shown for 3 carriers (*blue profile*) and compared to healthy eyes (*green profile*) (**C**, *below*).

Fig. S1B), the mean of the differences was 2.64 (±14.5) and the 95% limits of agreement between observers was −25.8 to 31.1.

The logMAR-equivalent BCVA ranged from 0 to 0.87. The group with the preserved NIR-AF signal associated with a preserved retinal island (10 patients) had a better mean visual acuity (mean logMAR equivalent [±SD], 0.16 ± 0.1) compared to the group with absent NIR-AF signal (logMAR equivalent [±SD], 0.46 ± 0.2) (6 patients), and the difference proved to be statistically significant ($P = 0.003$, Wilcoxon-Mann-Whitney Test).

Discussion

In gene therapy trials for CHM, favorable outcomes after gene replacement are considered more likely if the patients selected for the clinical trial present with central retinal islands having preserved RPE.[34] Thus, in a previously unexplored approach, we quantified the melanin signal originating primarily from RPE and captured by the NIR-AF imaging platform to detect RPE within preserved retinal islands in CHM. The importance of distinguishing RPE intactness is reinforced by our finding that mean visual acuity was higher in patients exhibiting NIR-AF signal.

Preserved retinal islands of variable size in P15, P5, and P7 (Fig. 1) were distinguished by the presence of SW-AF and NIR-AF signals, intact or discontinuous IZ and EZ reflectivity bands attributable to photoreceptor cells, and the absence of hypertransmission into the choroid. Taken together, these features indicated that RPE and photoreceptor cells were at least partially intact.

In association with preserved retinal islands at other locations, we observed that SW-AF signal could coexist with absent or appreciably reduced NIR-AF signal. For instance, in P6, the loss of RPE in residual fovea was indicated by the deficiency in NIR-AF signal and hypertransmission of OCT signal into the choroid due to reduced reflectance by RPE melanin (Figs. 1B, 1D). Nonetheless, an area of speckled SW-AF signal was also visible (Fig. 1C). A comparable but smaller area of SW-AF emission was detected in the fundus of P5, even as the NIR-AF signal was diminished (Figs. 1B, 1C). In the SD-OCT scan associated with this area, EZ and ELM were discontinuous, and hypertransmission into the choroid was observed (Fig. 1D).

These signs of RPE atrophy (reduced or absent NIR-AF with hypertransmission into the choroid) concomitant with the presence of a SW-AF signal are inconsistent with the assumption that SW-AF originates only from RPE cells. An alternative source of this aberrant SW-AF signal[39] is degenerating photoreceptor cells that are represented in P6 by the discontinuous IZ, EZ, and ELM reflectivity layers in SD-OCT images (Fig. 1D). Even in healthy eyes, the fluorophores of SW-AF form in photoreceptor cells before phagocytic transfer to RPE.[36] Accordingly, in the absence of NIR-AF, the SW-AF emission may originate from the photoreceptor outer and inner segments that are degenerating secondary to RPE atrophy. In support of this explanation, we have noted that elevated SW-AF in the absence of NIR-AF signal is also observed at positions of SD-OCT-detectable photoreceptor cell degeneration in other retinal disorders.[39,40]

In NIR-AF images of CHM-affected patients, we also observed melanin signal in zones where there was decidedly no SW-AF signal. Without the availability of an NIR-AF image, a residual island in P7 (Fig. 1B) might have been overlooked. In this example presented for P7 (Figs. 1A–D), hyperpigmentation in color fundus photographs colocalized with a veil of AF in the NIR-AF images, an absence of SW-AF, thinned ONL, a loss of EZ and ELM reflectivity layers, and the presence of an ORT, yet no hypertransmission into the choroid in the SD-OCT scan. A zone having NIR-AF emission in P6 is also devoid of SW-AF (Figs. 1B–D). One might suggest that the AF findings indicated the presence of RPE that had retained melanin (the NIR-AF signal) but were devoid of lipofuscin (absence of SW-AF signal). However, because SW-AF is attenuated by RPE melanin, it is also possible that the reduced SW-AF signal is a product of increased melanin absorbance of the SW-AF exciting light.

Interestingly, we found that qAF intensities mapped to the fundus by scaled color-coding were profoundly reduced not only in CHM-affected patients but also in female CHM carriers. As demonstrated in CHM carrier 1 (Fig. 4A), this qAF reduction was not attributable to outer retinal degeneration in SD-OCT scans (Fig. 2A). Moreover, the signal intensity was nonuniform in both NIR-AF and SW-AF images. Specifically, in CHM carriers, patches of reduced AF in SW-AF images colocalized with reduced AF in NIR-AF images. It has been suggested that nonuniform melanin distribution associated with CHM/REP-1 dysfunction represents an X-linked manifestation of altered RPE melanosome movement.[10] However, we have also studied melanin pigment mosaicism in NIR-AF images of X-linked albinism carriers (GPR143/OA1), and unlike in CHM carriers, patches of reduced signal in NIR-AF images of GPR143/OA1 carriers colocalize with increased signal (not reduced signal) in the SW-AF modality.[37] Moreover, because the fundus changes in CHM carriers develop with age[18] and exhibit progression,[41] random X-inactivation of REP-1 leading to melanosome dysfunctioning[10] is not sufficient to explain the mosaicism. This is an interesting issue that we are currently exploring. Whether RPE cells or photoreceptor cells are the first to express the disease has been an issue of uncertainty. We observed that choroidal vasculature was preserved even in areas exhibiting outer retinal atrophy, as indicated by the loss of EZ and ELM and increased OCT signal transmission into the choroid (Fig. 1, P5), which is indicative of RPE loss.

Other observations indicate that a disease process takes place in the RPE layer before the photoreceptors are affected in CHM. For instance we observed ORTs in the outer retina of both CHM-affected patients and carriers. The formation of ORTs is considered to reflect a survival response by photoreceptors, is particularly common under conditions such as geographic atrophy that originates in RPE, and is considered to be a reaction to loss or separation of photoreceptor cells from RPE.[42] Other structural changes in the outer retina that characterize late-onset retinal degeneration[43] have also been reported in carriers of CHM.[11] This is significant because late-onset retinal degeneration is caused by mutations in the gene C1QTNF5, which encodes a protein expressed by RPE.[44] This too suggests that RPE may be the primary site of the disease. We also note that despite the presence of NIR-AF emission from some central retinal islands, overall, the analysis of NIR-AF profiles through the fovea indicated that the signal was lower than in healthy eyes.

A limitation of this study is the relatively small cohort, with age trending toward older subjects. The inclusion of children or young adults would have allowed us to evaluate retina at earlier stages of disease. Additionally, we did not have specimens that would have allowed us to correlate SW-AF, NIR-AF, and SD-OCT findings with histopathologic changes.

The detection of preserved retinal islands in SW-AF images of CHM-affected patients has been used to evaluate disease progression in CHM.[29] The presence of RPE in these islands favors better visual acuity. Yet, we observed here that without the availability of NIR-AF images, SW-AF images can be misleading. We concur with a recent report that NIR-AF is valuable for patient selection and as an outcome measure in clinical trials.[45]

Acknowledgments

Supported by grants from the National Eye Institute RO1EY024091 (JRS) and P30EY019007; the Global Ophthalmology Awards

Program (GOAP), a Bayer-sponsored initiative committed to supporting ophthalmic research across the world; and a grant from Research to Prevent Blindness to the Department of Ophthalmology, Columbia University, New York, New York, United States.

Disclosure: **M. Paavo**, None; **J.R.L. Carvalho Jr**, None; **W. Lee**, None; **J.D. Sengillo**, None; **S.H. Tsang**, None; **J.R. Sparrow**, None

References

1. Zinkernagel MS, MacLaren RE. Recent advances and future prospects in choroideremia. *Clin Ophthalmol*. 2015;9:2195–2200.
2. Simunovic MP, Jolly JK, Xue K, et al. The spectrum of CHM gene mutations in choroideremia and their relationship to clinical phenotype. *Invest Ophthalmol Vis Sci*. 2016;57:6033–6039.
3. McTaggart KE, Tran M, Mah DY, Lai SW, Nesslinger NJ, MacDonald IM. Mutational analysis of patients with the diagnosis of choroideremia. *Hum Mutat*. 2002;20:189–196.
4. Cremers FP, van de Pol DJ, van Kerkhoff LP, Wieringa B, Ropers HH. Cloning of a gene that is rearranged in patients with choroideraemia. *Nature*. 1990;347:674–677.
5. Syed N, Smith JE, John SK, Seabra MC, Aguirre GD, Milam AH. Evaluation of retinal photoreceptors and pigment epithelium in a female carrier of choroideremia. *Ophthalmology*. 2001;108:711–720.
6. Gordiyenko NV, Fariss RN, Zhi C, MacDonald IM. Silencing of the CHM gene alters phagocytic and secretory pathways in the retinal pigment epithelium. *Invest Ophthalmol Vis Sci*. 2010;51:1143–1150.
7. Preising M, Ayuso C. Rab escort protein 1 (REP1) in intracellular traffic: a functional and pathophysiological overview. *Ophthalmic Genet*. 2004;25:101–110.
8. Pereira-Leal JB, Hume AN, Seabra MC. Prenylation of Rab GTPases: molecular mechanisms and involvement in genetic disease. *FEBS Lett*. 2001;498:197–200.
9. Seabra MC, Mules EH, Hume AN. GTPases, Rab intracellular traffic and disease. *Trends Mol Med*. 2002;8:23–30.
10. Futter CE, Ramalho JS, Jaissle GB, Seeliger MW, Seabra MC. The role of Rab27a in the regulation of melanosome distribution within retinal pigment epithelial cells. *Mol Biol Cell*. 2004;15:2264–2275.
11. Huang AS, Kim LA, Fawzi AA. Clinical characteristics of a large choroideremia pedigree carrying a novel CHM mutation. *Arch Ophthalmol*. 2012;130:1184–1189.
12. Jolly JK, Xue K, Edwards TL, Groppe M, MacLaren RE. Characterizing the natural history of visual function in choroideremia using microperimetry and multimodal retinal imaging. *Invest Ophthalmol Vis Sci*. 2017;58:5575–5583.
13. Aleman TS, Han G, Serrano LW, et al. Natural history of the central structural abnormalities in choroideremia: a prospective cross-sectional study. *Ophthalmology*. 2017;124:359–373.
14. Jacobson SG, Cideciyan AV, Sumaroka A, et al. Remodeling of the human retina in choroideremia: rab escort protein 1 (REP-1) mutations. *Invest Ophthalmol Vis Sci*. 2006;47:4113–4120.
15. Roberts MF, Fishman GA, Roberts DK, et al. Retrospective, longitudinal, and cross sectional study of visual acuity impairment in choroideraemia. *Br J Ophthalmol*. 2002;86:658–662.
16. Sieving PA, Niffenegger JH, Berson EL. Electroretinographic findings in selected pedigrees with choroideremia. *Am J Ophthalmol*. 1986;101:361–367.
17. Murro V, Mucciolo DP, Passerini I, et al. Retinal dystrophy and subretinal drusenoid deposits in female choroideremia carriers. *Graefes Arch Clin Exp Ophthalmol*. 2017;255:2099–2111.
18. Renner AB, Fiebig BS, Cropp E, Weber BH, Kellner U. Progression of retinal pigment epithelial alterations during long-term follow-up in female carriers of choroideremia and report of a novel CHM mutation. *Arch Ophthalmol*. 2009;127:907–912.
19. Preising MN, Wegscheider E, Friedburg C, Poloschek CM, Wabbels BK, Lorenz B. Fundus autofluorescence in carriers of choroideremia and correlation with electrophysiologic and psychophysical data. *Ophthalmology*. 2009;116:1201–1209e1 -2.
20. Vajaranant TS, Fishman GA, Szlyk JP, Grant-Jordan P, Lindeman M, Seiple W. Detection of mosaic retinal dysfunction in choroideremia carriers electroretinographic and psychophysical testing. *Ophthalmology*. 2008;115:723–729.
21. MacDonald IM, Russell L, Chan CC. Choroideremia: new findings from ocular pathology and review of recent literature. *Surv Ophthalmol*. 2009;54:401–407.
22. Tolmachova T, Anders R, Abrink M, et al. Independent degeneration of photoreceptors and retinal pigment epithelium in conditional knockout mouse models of choroideremia. *J Clin Invest*. 2006;116:386–394.
23. Flannery JG, Bird AC, Farber DB, Weleber RG, Bok D. A histopathologic study of a choroideremia carrier. *Invest Ophthalmol Vis Sci*. 1990;31:229–236.
24. Tolmachova T, Wavre-Shapton ST, Barnard AR, MacLaren RE, Futter CE, Seabra MC. Retinal pigment epithelium defects accelerate photoreceptor degeneration in cell type-specific knockout mouse models of choroideremia. *Invest Ophthalmol Vis Sci*. 2010;51:4913–4920.
25. Morgan JI, Han G, Klinman E, et al. High-resolution adaptive optics retinal imaging of cellular structure in choroideremia. *Invest Ophthalmol Vis Sci*. 2014;55:6381–6397.
26. Xue K, Oldani M, Jolly JK, et al. Correlation of optical coherence tomography and autofluorescence in the outer retina and choroid of patients with choroideremia. *Invest Ophthalmol Vis Sci*. 2016;57:3674–3684.
27. Sun LW, Johnson RD, Williams V, et al. Multimodal imaging of photoreceptor structure in choroideremia. *PLoS One*. 2016;11:e0167526.
28. Dysli C, Wolf S, Tran HV, Zinkernagel MS. Autofluorescence lifetimes in patients with choroideremia identify photoreceptors in areas with retinal pigment epithelium atrophy. *Invest Ophthalmol Vis Sci*. 2016;57:6714–6721.
29. Hariri AH, Velaga SB, Girach A, et al. Measurement and reproducibility of preserved ellipsoid zone area and preserved retinal pigment epithelium area in eyes with choroideremia. *Am J Ophthalmol*. 2017;179:110–117.
30. Syed R, Sundquist SM, Ratnam K, et al. High-resolution images of retinal structure in patients with choroideremia. *Invest Ophthalmol Vis Sci*. 2013;54:950–961.
31. MacLaren RE, Groppe M, Barnard AR, et al. Retinal gene therapy in patients with choroideremia: initial findings from a phase 1/2 clinical trial. *Lancet*. 2014;383:1129–1137.
32. Dimopoulos IS, Hoang SC, Radziwon A, et al. Two-year results after AAV2-mediated gene therapy for choroideremia: the Alberta experience. *Am J Ophthalmol*. 2018;193:130–142.
33. Lam BL, Davis JL, Gregori NZ, et al. Choroideremia gene therapy phase 2 clinical trial: 24-month results. *Am J Ophthalmol*. 2019;197:65–73.
34. Xue K, Jolly JK, Barnard AR, et al. Beneficial effects on vision in patients undergoing retinal gene therapy for choroideremia. *Nat Med*. 2018;24:1507–1512.
35. Keilhauer CN, Delori FC. Near-infrared autofluorescence imaging of the fundus: visualization of ocular melanin. *Invest Ophthalmol Vis Sci*. 2006;47:3556–3564.

36. Sparrow JR, Gregory-Roberts E, Yamamoto K, et al. The bisretinoids of retinal pigment epithelium. *Prog Retin Eye Res*. 2012;31:121–135.
37. Paavo M, Zhao J, Kim HJ, et al. Mutations in GPR143/OA1 and ABCA4 inform interpretations of short-wavelength and near-infrared fundus autofluorescence. *Invest Ophthalmol Vis Sci*. 2018;59:2459–2469.
38. Greenberg JP, Duncker T, Woods RL, Smith RT, Sparrow JR, Delori FC. Quantitative fundus autofluorescence in healthy eyes. *Invest Ophthalmol Vis Sci*. 2013;54:5684–5693.
39. Sparrow JR, Marsiglia M, Allikmets R, et al. Flecks in recessive Stargardt disease: short-wavelength autofluorescence, near-infrared autofluorescence, and optical coherence tomography. *Invest Ophthalmol Vis Sci*. 2015;56:5029–5039.
40. Boudreault KA, Schuerch K, Zhao J, et al. Quantitative autofluorescence intensities in acute zonal occult outer retinopathy vs healthy eyes. *JAMA Ophthalmol*. 2017;135:1330–1338.
41. MacDonald IM, Sui R, Zein W. Lines of Blaschko and choroideremia. *Ophthalmology*. 2009;116:1017–1018; author reply 1018.
42. Preti RC, Govetto A, Filho RGA, et al. Optical coherence tomography analysis of outer retinal tubulations: sequential evolution and pathophysiological insights. *Retina*. 2018;38:1518–1525.
43. Cukras C, Flamendorf J, Wong WT, Ayyagari R, Cunningham D, Sieving PA. Longitudinal structural changes in late-onset retinal degeneration. *Retina*. 2016;36:2348–2356.
44. Ayyagari R, Mandal MN, Karoukis AJ, et al. Late-onset macular degeneration and long anterior lens zonules result from a CTRP5 gene mutation. *Invest Ophthalmol Vis Sci*. 2005;46:3363–3371.
45. Birtel J, Salvetti AP, Jolly JK, et al. Near-infrared autofluorescence in choroideremia: anatomic and functional correlations. *Am J Ophthalmol*. 2019;199:19–27.

Investigative Ophthalmology & Visual Science